ELSEVIER

Contents lists available at ScienceDirect

Computers and Mathematics with Applications

journal homepage: www.elsevier.com/locate/camwa





Moving interfaces in peridynamic diffusion models and the influence of discontinuous initial conditions: Numerical stability and convergence

Francesco Scabbia ^a, Claudia Gasparrini ^b, Mirco Zaccariotto ^{a,c}, Ugo Galvanetto ^{a,c}, Adam Larios ^d, Florin Bobaru ^{e,*}

- ^a Center of Studies and Activities for Space (CISAS) "G. Colombo", via Venezia 15, Padova, 35131, Italy
- b Department of Materials and Centre for Nuclear Engineering, Imperial College London, Exhibition Road, London SW 7 2AZ, United Kingdom
- ^c Department of Industrial Engineering, University of Padova, via Venezia 1, Padova, 35131, Italy
- d Department of Mathematics, University of Nebraska-Lincoln, Lincoln, NE 68588-0130, USA
- c Department of Mechanical and Materials Engineering, University of Nebraska-Lincoln, Lincoln, NE, 68588-0526, USA

ARTICLE INFO

Keywords: Peridynamics Diffusion-reaction problem Numerical stability Discontinuous initial conditions Phase change Moving interface

ABSTRACT

We derive numerical stability conditions and analyze convergence to analytical nonlocal solutions of 1D peridynamic models for transient diffusion with and without a moving interface. In heat transfer or oxidation, for example, one often encounters initial conditions that are discontinuous, as in thermal shock or sudden exposure to oxygen. We study the numerical error in these models with continuous and discontinuous initial conditions and determine that the initial discontinuities lead to lower convergence rates, but this issue is present at early times only. Except for the early times, the convergence rates of models with continuous and discontinuous initial conditions are the same. In problems with moving interfaces, we show that the numerical solution captures the exact interface location well, in time. These results can be used in simulating a variety of reaction-diffusion type problems, such as the oxidation-induced damage in zirconium carbide at high temperatures.

1. Introduction

Discontinuities are difficult to handle in classical models involving partial differential equations (PDEs). Nonetheless, discontinuities take place in many physical phenomena in nature, such as fracture, thermal shock in heat transfer, or oxidation-induced damage. For problems with moving interfaces, classical theories do require special treatment to govern the motion of the interface, such as the Stefan condition [1-4]. The peridynamic theory has been proven to effectively solve these types of problems without any ad-hoc conditions at the interface: the motion of the interface is implicitly determined by the diffusion and phase properties of the involved materials, as shown in, for example, [3,5]. Another important problem in which moving interfaces are involved in conjunction with fracture is the problem of oxidation-induced fracture in high temperature zirconium-carbide [6,7]. To study these types of problems, one needs numerical approximations of transient diffusion with moving interfaces. In this work we analyze the stability of the so-called "meshfree method" for discretizing peridynamic models, the influence of discontinuous initial conditions (due to, for example, sudden exposure of the body to a non-zero temperature/concentration), and the accuracy of the numerical solution for transient diffusion problems with a moving interface.

Peridynamics (PD) is a non-local continuum theory able to model discontinuities in a mathematically consistent way [8,9]. In the peridynamic formulation, the spatial derivatives of the PDEs are replaced by integrals over a sphere of radius $\delta > 0$. The so-called *horizon size* δ is the measure of nonlocality of the theory, i.e., the maximum distance at which two points interact with each other. This PD interaction is named *hond*

It is well-known that in peridynamic models the behavior in that region is different from the behavior in the bulk since points close to the boundary of the domain have an incomplete horizon region. This phenomenon is known as the *PD surface effect* [10–15]. The properties of the interactions of the points near the boundary can be modified to mitigate the PD surface effect with several methods [10,16–20,13]. However, the results obtained with these methods may still exhibit some residual fluctuations, depending on how the PD boundary conditions are applied.

^{*} Corresponding author.

E-mail address: fbobaru2@unl.edu (F. Bobaru).

Boundary conditions in local models are applied at the domain boundary, whereas nonlocal boundary conditions need to be specified over a boundary layer of finite thickness. This is the reason why the nonlocal boundary conditions are sometimes called volume constraints [21]. However, since experiments provide only local measurements at the boundary of the domain, it is often desirable to impose local boundary conditions in a nonlocal model. To do so, several methods have been developed. For instance, the interior of the body could be modeled with PD and the layer near the external surface of the body with a classical model, but only if discontinuities do not arise in this layer of material. To do so, a coupling method is required (see, e.g., [22-30]), which may lead to spurious effects at the interface of the coupling region due to the different (local and nonlocal) formulations [31]. Another approach is reducing the nonlocal radius δ with the variable horizon method (see, e.g., [32,11,33–37]), so that $\delta \to 0$ at the boundary. However, in this case, for transient problems, for example, material length-scales may not be matched (e.g., wave dispersion will be different near the surface compared to in the bulk in elasto-dynamic problems). The fictitious node method is the most commonly used to impose local boundary conditions in a nonlocal model (see, e.g., [38,16,17,39-44,13,36,45,37,14,46,15,47]): a fictitious layer is added all around the body, to complete the horizon region for nodes in the PD boundary layer, and is used to impose the PD boundary conditions. Among all these methods, here we employ the "surface node" method (SNM) [14,15,47] because it provides a problem-independent, accurate way to impose local boundary conditions in a PD model for any loading conditions and (even complex) geometry.

The peridynamic theory has been already successfully applied to simple diffusion problems [48,49] and more complex phenomena (for instance, diffusion coupled with corrosion mechanisms [3,5]). However, some numerical aspects have not been studied yet:

- a stability criterion for time-integration of PD diffusion equations accounting for the boundary conditions applied; existing stability results were limited to von Neumann analysis which assumes infinite domain;
- the influence of discontinuities in initial conditions on the accuracy of the numerical solution;
- the accuracy of numerical solutions for diffusion-type problems with moving interfaces.

To investigate these issues in a simple framework, we analyze several 1D examples, but the obtained conclusions may be generalized to higher-dimension problems. Moreover, for the first time, we apply the SNM to a time-dependent problem, and for discontinuous initial conditions. The stability of numerical methods has been observed to be considerably affected by the behavior of the system near the boundaries due to the high gradients imposed by the boundary conditions (such as in the case of no-slip boundary conditions in Navier-Stokes equations [50,51], for example). Therefore, including the effect of the surface node method near the boundaries of the body is critically important for deriving an accurate stability criterion.

The paper is structured as follows. Section 2 gives a brief review of the peridynamic theory applied to diffusion problems with or without moving interfaces, and their discretized equations. In Section 3, we derive the stability criterion for peridynamic diffusion problems by including the influence of boundary conditions. Section 4 presents the numerical results of a 1D diffusion problem for a homogeneous material with no phase changes and, for the first time, the surface node method for enforcing nonlocal boundary conditions is applied to a transient problem. We then analyze the numerical convergence to an exact nonlocal solution of a PD model for initial conditions with and without discontinuities. Section 5 shows an example of a diffusion-type model with a moving interface problem in which the motion of the interface is controlled by local concentration values, similar to diffusion in a bi-material enhanced with a phase-change model in [3], as some PD

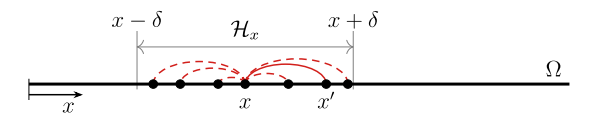


Fig. 1. Neighborhood \mathcal{H}_x of a point in a peridynamic body Ω in 1D: red lines represent the PD interactions (bonds) between points.

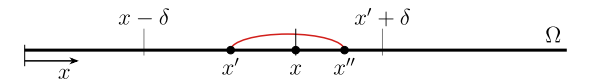


Fig. 2. Example of a bond involved in the computation of the peridynamic flux in a point x: for the limits of integration in equation (2), x' and x'' are points respectively in the intervals $[x-\delta,x]$ and $[x,x'+\delta]$, therefore each bond between x' and x'' intersects the surface passing through point x.

models of corrosion have employed. The results are compared with an analytical solution (obtained via the manufactured solution method) for a moving interface problem. Section 6 discusses extensions of the obtained results in 1D problems to the 2D and 3D cases. Section 7 draws some conclusions and discusses future work.

2. Brief review of PD model of diffusion

In peridynamics, points in a body Ω interact with each other up to a finite distance δ , called the *horizon size* [8,9]. The interaction between two points is called *bond*. This means that a point x interacts with the set of points $\mathcal{H}_x = \{x' \in \Omega : |x' - x| < \delta\}$, which is called the *neighborhood* of point x. Therefore, the neighborhood is the set $[x - \delta, x + \delta]$, as shown in Fig. 1. The peridynamic equation governing diffusion phenomena is given as in [3,5]:

$$\frac{\partial C(x,t)}{\partial t} = \int_{\mathcal{H}_x} d(x,x') \,\mu(|x'-x|) \big[C(x',t) - C(x,t) \big] \,\mathrm{d}x'$$

$$= \int_{\mathcal{H}_x} \mathbf{j}(x,x',t) \,\mathrm{d}x',$$
(1)

where C is the concentration of the species, μ is the kernel function, and d is the micro-diffusivity (that can be calibrated to the classical diffusivity). The integrand in equation (1) is called the *micro-flux* $\mathbf{j}(x,x',t)$. We choose the kernel function $\mu(|x'-x|) = |x'-x|^{-2}$, which ensures that the convergence to the classical theory does not depend on the refinement of the nodal grid [41].

Each bond can be thought as a pipe into which the monitored species is allowed to flow. The peridynamic flux at a point is defined as the sum of the micro-fluxes of the bonds crossing the surface passing through that point [52]. Therefore, in 1D the PD flux at a point x is computed as [14]:

$$J(x,t) = -\int_{x-\delta}^{x} \int_{x}^{x'+\delta} j(x',x'',t) dx'' dx'.$$
 (2)

Fig. 2 shows the limits of integration accounting for each bond intersecting the surface passing through point x.

The micro-diffusivity function d is calibrated to the classical diffusivity D. To do so, for example, one equates the classical flux with the peridynamic flux for a linear distribution of concentration C [48,49,3]. The peridynamic flux at a point x with a complete neighborhood (away from the boundaries of the domain) for a homogeneous concentration gradient is computed as [15,48]:

$$J(x,t) = -\int_{x}^{x+\delta} \left(x'-x\right) \mathbf{j}(x,x',t) \, \mathrm{d}x'. \tag{3}$$

Therefore, by choosing a constant micro-diffusivity function over the neighborhood [48,49,3], the micro-diffusivity of a PD bond is given as:

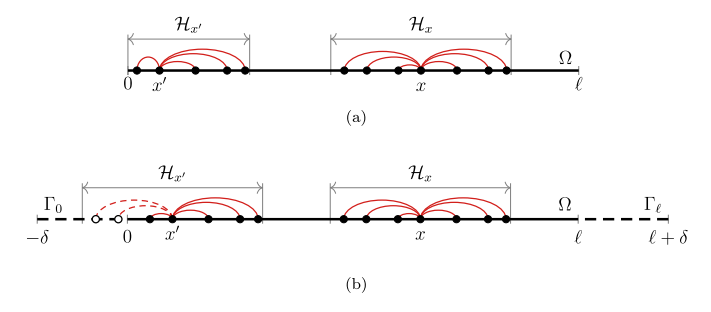


Fig. 3. In order to complete the neighborhoods of the points near the boundary (a), a fictitious layer $\Gamma = \Gamma_0 + \Gamma_\ell$ surrounding the body Ω is introduced (b).

$$d(x, x') = \frac{D}{s}. (4)$$

Since equation (4) is computed for points with a complete neighborhood, the properties of the points near the boundary of the body (with an incomplete neighborhood) turn out to be different from those of the points in the bulk (see Fig. 3a). This phenomenon is called PD surface effect [13-15]. In order to mitigate this surface effect, a fictitious layer, of thickness δ , surrounding the body is introduced as first suggested in [38] (see Fig. 3b). Furthermore, nonlocal models require the imposition of nonlocal boundary conditions, also known as volume constraints. However, experiments provide only measurements at the boundary of the domain, so the imposition of local boundary conditions is desirable. In order to enforce a set of local boundary conditions into a nonlocal model, several methods have been developed (see, e.g., [17,19,37,45]). However, all these methods do not guarantee the accuracy of the results near the boundaries for any loading condition or complex geometry. On the other hand, the surface node method (see, e.g., [14,15,47]) provides an accurate way to impose local boundary conditions in a nonlocal model for any loading condition and geometry (for any domain with sufficiently smooth boundary). According to this method, concentrations of the fictitious nodes are determined by a Taylor series expansion about the closest point on the external surface of the body. Then, the flux at points on the external surface of the body is imposed via the equation of the peridynamic flux:

$$J(x, \mathbf{n}, t) = J(x, t) \cdot \mathbf{n}, \tag{5}$$

where $n=\pm 1$ is the unit vector normal to the external surface. Thanks to this equation, the points on the boundary represent the nonlocal behavior of the entire fictitious layer; this aspect will be explained in detail in the discretized model in Section 2.2.

2.1. Modeling of diffusion with moving interface/phase-change

Diffusion-controlled or reaction-controlled problems are involved in many physical phenomena. Oxidation of zirconium carbide at high temperatures is one such example [6,7]. The diffusion of oxygen within the high-temperature zirconium carbide triggers oxidation, the final products of which are carbon dioxide and zirconium oxide. The carbon dioxide is dispersed in the external environment (through cracks or porosities). The interface between zirconium oxide and carbide moves according to the diffusivities of the two phases. This phenomenon can be described as a diffusion problem in a bi-material enhanced with a phase-change model, which was analyzed in [3].

The phase of each peridynamic point depends on its current concentration. Let us denote the concentration of phase change by C_i , where i stands for "interface". The micro-diffusivity of a bond is determined as [3]:

$$d(x, x', t) = \begin{cases} d_1 & \text{if } C(x, t) < C_i \text{ and } C(x', t) < C_i, \\ d_2 & \text{if } C(x, t) > C_i \text{ and } C(x', t) > C_i, \\ d_3 & \text{if } C(x, t) \le C_i \le C(x', t) \text{ or } C(x', t) \le C_i \le C(x, t). \end{cases}$$
(6)



Fig. 4. Three possible types of bonds for diffusion in a two-phase material separated by a material interface: each type of bond may have different micro-diffusivity properties.

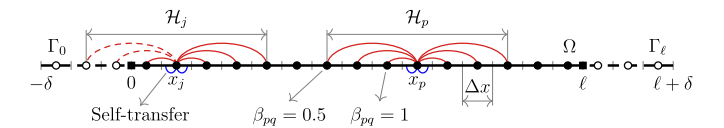


Fig. 5. Discretization of a 1D body by means of the meshfree method: the neighborhood \mathcal{H}_p of a node p (or \mathcal{H}_j of a node j) is constituted by the nodes with a portion of their cell within the neighborhood. The quadrature coefficient β_{pq} is the volume fraction of the cell of node q lying inside the neighborhood of node p [62]. The fictitious nodes (empty dots) are added near the boundary of the body to complete the neighborhoods of all the nodes within the body (solid dots). Moreover, the boundary of the body is represented by the surface nodes (solid squares).

Fig. 4 shows the three possible types of bonds that may have different micro-diffusivities properties. Therefore, in a peridynamic diffusion model, it suffices to know the threshold concentration for phase change and the micro-diffusivities in equation (6) in order to determine the motion of the interface. With this, the motion of the interface is autonomous, and determined by the "constitutive model" itself. Note that this model does not require any special conditions at the interface, such as Stefan condition (that is instead required in classical models [1,2,4]). Moreover, a damage mechanism can be easily introduced in this PD model (see for instance [3,53,5,54–58]). This will be investigated in a future work [59].

2.2. The "meshfree method" discretization of the PD diffusion equations

Many different methods can be used to discretize peridynamic diffusion equations, such as the "meshfree method" [60-62], the Finite Element Method (FEM) [63,64], and the Fast Convolution-Based Method (FCBM) [65,66]. When using the FEM, remeshing would be required to model the moving interface. The FCBM allows to considerably reduce the computational cost of finding PD solutions by utilizing the convolutional structure of PD integral operators and the Fast Fourier Transform (FFT). However, since in this work we consider stability and convergence of numerical algorithms in the 1D setting for which the cost is less of an issue, for the sake of simplicity we here adopt the meshfree method of discretization of the PD equations, and we use uniform grids. Therefore, the body is discretized in cells (segments), at the center of each of which there is a node representing that cell. To mitigate the PD surface effect, we add the fictitious nodes around the body up to a distance δ from the boundary (see Fig. 5). The concentrations of the fictitious nodes can be determined via the Taylor-based extrapolation [14,15,47] or some other type of extrapolation (see, e.g., [37,45]). In this work, we use the Taylor-based method with linear extrapolation for its simplicity.

The integrals in the peridynamic equations (equations (1) and (2)) can be numerically approximated by splitting them into a summation of integrals over cells and applying a midpoint quadrature rule in each cell [60-62]. Therefore, the micro-flux in a bond between the nodes p and q can be computed as:

$$j(x_p, x_q, t) = d(x_p, x_q) \, \mu(|x_q - x_p|) \left[C(x_q, t) - C(x_p, t) \right], \tag{7}$$

where x_p and x_q are the coordinates respectively of nodes p and q, and $\mu(|x_q-x_p|)=|x_q-x_p|^{-2}$.

As shown in Fig. 5, the cells of some nodes are contained only partially within the neighborhood. In order to properly "weight" their contribution, the quadrature coefficients β are computed as the fraction

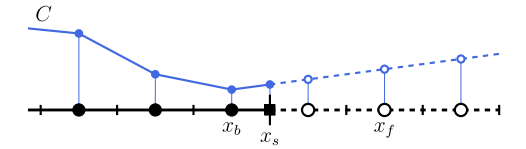


Fig. 6. Example of the linear Taylor-based extrapolation applied to an arbitrary concentration field.

of the nodal cell lying inside the neighborhood using the algorithms presented in [11]. Hence, a node p within the body is governed by the following discretized equation [48,49,3]:

$$\frac{\partial C(x_p, t)}{\partial t} = \sum_{q \in \mathcal{H}_p} \mathbf{j}(x_p, x_q, t) \, \beta_{pq} \Delta x + \mathbf{j}_{st}(x_p, t) \Delta x, \tag{8}$$

where Δx is the grid spacing, the index q stands for any node within the neighborhood \mathcal{H}_p of node p, and j_{st} is the so-called *self-transfer* micro-flux. This self-transfer term appears in equation (8) due to the discretization of the body. In fact, the "discretized" neighborhood \mathcal{H}_p lacks the central portion because the node x_p does not interact with the two halves of its own cell. As shown in Fig. 5, the self-transfer is added to take into account these lacking contributions. The self-transfer micro-flux of node p can be approximated as the average of the micro-fluxes of the two adjacent nodes [41]:

$$\begin{split} \mathbf{j}_{st}(x_p,t) &= \frac{1}{2} \left[d(x_p,x_{p+1}) \, \mu(|x_{p+1}-x_p|) \big(C(x_{p+1},t) - C(x_p,t) \big) \right. \\ &+ d(x_p,x_{p-1}) \, \mu(|x_{p-1}-x_p|) \big(C(x_{p-1},t) - C(x_p,t) \big) \right], \end{split} \tag{9}$$

where the sequential numbering of the nodes is assumed, so that nodes p-1 and p+1 are the two nodes adjacent to node p.

Let us call *interior nodes* the nodes within the body (solid dots in Fig. 5). To apply the surface node method (with the linear Taylor-based extrapolation) for imposing the boundary conditions, we introduce new nodes at the boundary of the body, called *surface nodes* (solid squares in Fig. 5). The surface nodes do *not* have cells as the interior nodes, but they are used to discretize the external surface of the body. In 1D the surface nodes are the points at the ends of the body, as shown in Fig. 5, and lie at a distance of $\Delta x/2$ from the closest interior node.

In order to complete the neighborhoods of the interior nodes near the boundaries, a δ -thick layer of fictitious nodes is introduced, as shown in Fig. 6. The concentration of these nodes is determined by extrapolating the concentrations of the real nodes. Different extrapolation methods may be employed, but the Taylor-based extrapolation method is straightforward and applicable to any (even complex) geometry [14,15,47]. Therefore, here we show how to extrapolate the concentrations of the fictitious nodes with a linear Taylor series expansion. Consider a fictitious node f and its closest surface node f and interior node f and respectively denote their coordinates by f0, f1, f2, f3 and f3, as shown in Fig. 6. The concentration of the fictitious node f3 is computed as:

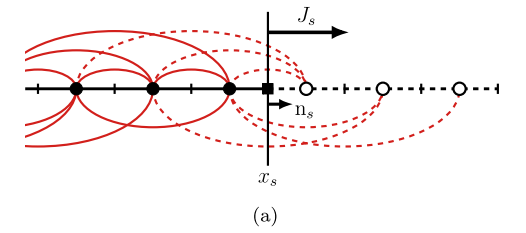
$$C(x_f, t) \approx C(x_s, t) + (x_f - x_s) \frac{\partial C(x_s, t)}{\partial x}$$

$$\approx C(x_s, t) + (x_f - x_s) \frac{C(x_s, t) - C(x_b, t)}{x_s - x_b}$$

$$\approx \frac{x_f - x_b}{x_s - x_b} C(x_s, t) - \frac{x_f - x_s}{x_s - x_b} C(x_b, t),$$
(10)

where the derivative $\frac{\partial C(x_s,t)}{\partial x}$ is approximated by the finite difference method. Note that the concentrations of the fictitious nodes are determined as functions of the concentrations of the real (both interior and surface) nodes of the body, which are often the unknowns of the problem. Fig. 6 shows an example of the linear Taylor-based extrapolation.

The surface nodes do *not* interact directly with other nodes. In other words, no PD bonds are connected to surface nodes. The degrees of freedom of the surface nodes are governed by new equations based on



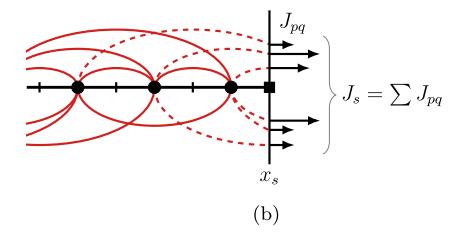


Fig. 7. Representation of the equation of a surface node s: (a) the flux $J_s = J(x_s, n_s, t)$ is computed as (b) the sum of the fluxes $J_{pq} = -\mathrm{j}(x_p, x_q, t) \cdot \mathrm{n}_s \, \beta_{pq} \, \Delta x^2$ of the bonds intersecting node s.

the concept of peridynamic flux. Therefore, the equation of a surface node x_s with normal n_s is given as [47]:

$$J(x_s, \mathbf{n}_s, t) = -\sum_{B_s} \mathbf{j}(x_p, x_q, t) \cdot \mathbf{n}_s \, \beta_{pq} \Delta x^2 \,, \tag{11}$$

where B_s is the set of all the bonds such that $x_p < x_s < x_q$, i.e., all the bonds crossing the boundary. These bonds are depicted in Fig. 7. Thus, the boundary conditions can be imposed directly on the surface nodes as one would do in a local model [47]: a constrained concentration $\overline{C}(t)$ at a surface node s is imposed as $C(x_s,t) = \overline{C}(t)$ and a flux $\overline{J}(t)$ through the cell of a surface node s is imposed as $J(x_s,n_s,t) = \overline{J}(t)$.

Thanks to equation (11), the surface nodes are affected by all the bonds connected to fictitious nodes (see Fig. 7). In fact, the bond fluxes that should be applied to the fictitious nodes, are instead applied to the surface node. Therefore, the surface nodes represent the nonlocal behavior of the whole fictitious layer. This is why the local boundary conditions imposed at the surface nodes can be seen as similar to volume constraints (nonlocal boundary conditions).

For the time integration, the forward Euler (first-order explicit) method is employed:

$$C_p^{n+1} = C_p^n + \Delta t \frac{\partial C_p^n}{\partial t}, \tag{12}$$

where the subscript and superscript stand respectively for the corresponding position of the node and time-step so that, for instance, $C_p^n = C(x_p, t_n)$. Therefore, the time integration is carried out by combining equations (7), (8) and (12) as:

$$\begin{split} C_{p}^{n+1} &= C_{p}^{n} + d\Delta t \sum_{q \in \mathcal{H}_{p}} \mu_{pq} \left(C_{q}^{n} - C_{p}^{n} \right) \beta_{pq} \Delta x \\ &+ \frac{1}{2} d \, \mu(\Delta x) \left(C_{p+1}^{n} - 2 C_{p}^{n} + C_{p-1}^{n} \right) \Delta x \end{split} \tag{13}$$

where *d* is computed with equation (4) and $\mu_{pq} = \mu(|x_q - x_p|)$. This system of equations can also be written in the matrix form as:

$$\mathbf{C}^{n+1} = \mathbf{A} \, \mathbf{C}^n \,, \tag{14}$$

where C^n and C^{n+1} are the concentration vectors at time-steps n and n+1, respectively.

3. Stability analysis

The stability analysis in peridynamic models has been carried out via the Von Neumann stability analysis for hyperbolic equations discretized with the meshfree method in [60,67] and for parabolic equa-

tions considering the fast convolution-based method in [65,66]. Note that this type of analysis considers only pure initial value problems and completely neglects the influence of the boundary conditions [68]. In [69,70] the stability condition of the forward Euler scheme applied to parabolic equations discretized in space with the finite element method is discussed. Here we follow the general analysis (that also includes the treatment of boundary conditions), known as the *eigenvalue technique* for stability analysis, to find the restriction on the time-step Δt for peridynamic parabolic equations discretized with the meshfree method.

A numerical method is semi-stable if the numerical errors do not grow as the solution progresses in time. According to the eigenvalue technique for stability analysis, the numerical method in equation (14) is semi-stable if the largest eigenvalue λ_{max} of the matrix ${\bf A}$ is such that $|\lambda_{max}| \leq 1$. In this work we consider a body under Dirichlet boundary conditions at both ends, i.e., at the surface nodes. Therefore, since the values of the concentrations at those nodes are known, the surface nodes do not contribute to the numerical errors. In order to bound the eigenvalues of matrix ${\bf A}$ with entries a_{ij} , we use the Gershgorin Theorem which states that each eigenvalue of ${\bf A}$ lies within at least one of the circles centered in a_{ii} with a radius $\sum_{j \neq i} |a_{ij}|$ (the so-called Gershgorin discs in the complex plane):

$$|\lambda - a_{ii}| \le \sum_{i \ne i} |a_{ij}|,\tag{15}$$

where a_{ii} and a_{ij} are the diagonal and off-diagonal entries of matrix **A**. The stability criterion without considering the influence of the boundary conditions and the self-transfer term is given as:

$$\Delta t \le \frac{1}{d \sum_{q \in \mathcal{H}_n} \mu_{pq} \, \Delta x} \,. \tag{16}$$

This inequality is obtained by applying the Gershgorin Theorem to the rows of matrix $\bf A$ corresponding to a generic node p lying in the bulk of the body, i.e. a node without fictitious nodes in its neighborhood (see the following proof). Note that, for simplicity's sake, the quadrature coefficient β is neglected in the determination of the upper bound for the time-step size. However, the entries of the rows of $\bf A$ corresponding to the nodes near the boundary of the body are different from those considered to obtain equation (16), due to the presence of the fictitious nodes inside the neighborhood of those nodes. In fact, some of the entries of $\bf A$ are modified according to the linear Taylor-based extrapolation (equation (10)). The tighter upper bound for the time-step size is found by applying the Gershgorin Theorem to the row of $\bf A$ corresponding to the interior node closest to the boundary, as shown in the following.

Theorem. For the peridynamic equation of transient diffusion discretized in space with the meshfree method and in time with the forward Euler scheme, in which the boundary conditions are imposed via the surface node method with a linear Taylor-based extrapolation, the stability condition is given as

$$\Delta t \le \frac{1}{d\left(\sum_{\alpha \in \mathcal{H}_{L}} \mu_{bq} + \frac{1}{2} \sum_{f \in \mathcal{H}_{L}} \mu_{bf} \left(\frac{x_{f} - x_{s}}{x_{s} - x_{b}} - 1\right)\right) \Delta x}$$

$$(17)$$

when the self-transfer term is not considered, and

$$\Delta t \le \frac{1}{d\left(\sum_{q \in \mathcal{H}_b} \mu_{bq} + \frac{1}{2} \sum_{f \in \mathcal{H}_b} \mu_{bf} \left(\frac{x_f - x_s}{x_s - x_b} - 1\right) + \frac{1}{2} \mu(\Delta x)\right) \Delta x}$$

$$(18)$$

when the self-transfer term is considered.

Proof. For simplicity and conciseness, we prove the stability condition in equation (17) without considering the self-transfer term. The upper bound for the time-step size, when the self-transfer term is considered, can be found following the same steps. For simplicity's sake, we also neglect the quadrature coefficients β in all the following formulas. If

 β was included in the analysis, the upper bound for the time-step size would slightly increase.

The concentration at a node p in the bulk of the body, i.e., a node without fictitious nodes within its neighborhood, at the time-step n + 1, is given as (see equation (13)):

$$C_p^{n+1} = \left[1 - d\Delta t \sum_{q \in \mathcal{H}_p} \mu_{pq} \Delta x \right] C_p^n + d\Delta t \sum_{q \in \mathcal{H}_p} \mu_{pq} C_q^n \Delta x, \tag{19}$$

where $\mu_{pq} = \mu(|x_q - x_p|)$. The Gershgorin Theorem applied to the rows of A corresponding to node p yields:

$$\left| \lambda - 1 + d\Delta t \sum_{q \in \mathcal{H}_n} \mu_{pq} \Delta x \right| \le \sum_{q \in \mathcal{H}_n} \left| d\Delta t \mu_{pq} \Delta x \right|. \tag{20}$$

Note that the terms within the summation on the right-hand side of this equation are always positive. Therefore, equation (20) becomes:

$$-d\Delta t \sum_{q \in \mathcal{H}_p} \mu_{pq} \Delta x \le \lambda - 1 + d\Delta t \sum_{q \in \mathcal{H}_p} \mu_{pq} \Delta x \le d\Delta t \sum_{q \in \mathcal{H}_p} \mu_{pq} \Delta x. \tag{21}$$

According to the eigenvalue technique, the stability of the numerical method is achieved when $-1 \le \lambda \le 1$. The right inequality yields $\lambda \le 1$, whereas the left inequality is:

$$\lambda \ge 1 - 2d\Delta t \sum_{q \in \mathcal{H}_{+}} \mu_{pq} \Delta x. \tag{22}$$

Thus, one obtains $\lambda \ge -1$ if the following condition holds:

$$\Delta t \le \frac{1}{d \sum_{q \in \mathcal{H}_n} \mu_{pq} \Delta x} \,. \tag{23}$$

This is the stability criterion for the choice of a stable time-step when no correction methods for the PD surface effect or the imposition of the nonlocal boundary conditions are used.

We consider now a node p having one or more fictitious nodes within its neighborhood. In equation (19), we subdivide the last summation over the nodes within the neighborhood of node p as the sum of the summations of the real (denoted with r) and fictitious (denoted with f) nodes within the neighborhood of node p:

$$C_p^{n+1} = \left[1 - d\Delta t \sum_{q \in \mathcal{H}_p} \mu_{pq} \Delta x\right] C_p^n + d\Delta t \sum_{r \in \mathcal{H}_p} \mu_{pr} C_r^n \Delta x + d\Delta t \sum_{f \in \mathcal{H}_p} \mu_{pf} C_f^n \Delta x.$$
(24)

As shown in Fig. 8, consider a surface node, named s, and the real node closest to it, named b. As dictated by the surface node method with a linear Taylor-based extrapolation [14,15,47], the concentration C_f^n of the fictitious nodes is computed with a linear Taylor series expansion as in equation (10). However, since there are no numerical errors at the surface nodes (where Dirichlet boundary conditions are imposed), we neglect the contributions to matrix \mathbf{A} of the concentrations C_s^n of the surface nodes. Hence, we obtain:

$$C_p^{n+1} = \left[1 - d\Delta t \sum_{q \in \mathcal{H}_p} \mu_{pq} \Delta x\right] C_p^n + d\Delta t \sum_{r \in \mathcal{H}_p} \mu_{pr} e_r^n \Delta x - d\Delta t \sum_{f \in \mathcal{H}_p} \mu_{pf} c_f C_b^n \Delta x\,,$$

(25)

where $c_f = \frac{x_f - x_s}{x_s - x_b}$ is a positive scalar value derived from equation (10). When $p \neq b$ (i.e., node p is not the interior node closest to the boundary):

F. Scabbia, C. Gasparrini, M. Zaccariotto et al.

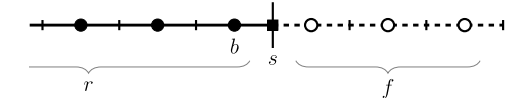


Fig. 8. Notation used for the indices of the nodes for the stability analysis: r are the real nodes, f are the fictitious nodes, g is the surface node, and g is the real node closest to node g.

$$C_p^{n+1} = \left[1 - d\Delta t \sum_{q \in \mathcal{H}_p} \mu_{pq} \Delta x \right] C_p^n + d\Delta t \sum_{r \in \mathcal{H}_p - \{b\}} \mu_{pr} C_r^n \Delta x$$

$$+ d\Delta t \left[\mu_{pb} \Delta x - \sum_{f \in \mathcal{H}_p} \mu_{pf} c_f \Delta x \right] C_b^n,$$
(26)

The Gershgorin Theorem applied to this case yields:

$$\left| \lambda - 1 + d\Delta t \sum_{q \in \mathcal{H}_p} \mu_{pq} \Delta x \right| \le d\Delta t \left(\sum_{r \in \mathcal{H}_n - \{b\}} \mu_{pr} + \left| \mu_{pb} - \sum_{f \in \mathcal{H}_p} \mu_{pf} c_f \right| \right) \Delta x. \tag{27}$$

Following the same steps as before, the first inequality deriving from equation (27) is given as:

$$\lambda \le 1 + d\Delta t \left(-\sum_{q \in \mathcal{H}_p} \mu_{pq} + \sum_{r \in \mathcal{H}_p - \{b\}} \mu_{pr} + \left| \mu_{pb} - \sum_{f \in \mathcal{H}_p} \mu_{pf} c_f \right| \right) \Delta x. \tag{28}$$

Since the set of nodes in the neighborhood \mathcal{H}_p is the sum of the disjointed sets of real and fictitious nodes, the inequality is rewritten as:

$$\lambda \le 1 + d\Delta t \left(-\sum_{f \in \mathcal{H}_p} \mu_{pf} - \mu_{pb} + \left| \mu_{pb} - \sum_{f \in \mathcal{H}_p} \mu_{pf} c_f \right| \right) \Delta x. \tag{29}$$

We have that $\lambda \le 1$ if the following condition holds:

$$-\sum_{f\in\mathcal{H}_{p}}\mu_{pf} - \mu_{pb} + \left|\mu_{pb} - \sum_{f\in\mathcal{H}_{p}}\mu_{pf}c_{f}\right| \le 0,$$
(30)

which leads to:

$$-\sum_{f \in \mathcal{H}_{p}} \mu_{pf} - \mu_{pb} \le \mu_{pb} - \sum_{f \in \mathcal{H}_{p}} \mu_{pf} c_{f} \le \sum_{f \in \mathcal{H}_{p}} \mu_{pf} + \mu_{pb}. \tag{31}$$

The right inequality is always true, whereas the left inequality becomes:

$$\mu_{pb} \ge \frac{1}{2} \sum_{f \in \mathcal{H}_p} \mu_{pf} \left(c_f - 1 \right) .$$
 (32)

Note that here no term depends on the time-step size Δt , but this inequality depends on the kernel μ and on how many fictitious nodes are present in the neighborhood of node p. Therefore, to satisfy the condition in equation (32), an appropriate kernel can be chosen or one can make use of a preconditioner to modify accordingly the entries of matrix **A**. If neither of the above options is adopted, the stability criterion still provides a good first guess for the time-step size.

The second inequality deriving from equation (27) is given as:

$$\lambda \ge 1 - d\Delta t \left(\sum_{q \in \mathcal{H}_n} \mu_{pq} + \sum_{r \in \mathcal{H}_n - \{b\}} \mu_{pr} + \left| \mu_{pb} - \sum_{f \in \mathcal{H}_n} \mu_{pf} c_f \right| \right) \Delta x. \tag{33}$$

Since $\lambda \ge -1$, the following condition holds:

$$d\Delta t \left(\sum_{q \in \mathcal{H}_p} \mu_{pq} + \sum_{r \in \mathcal{H}_p - \{b\}} \mu_{pr} + \left| \mu_{pb} - \sum_{f \in \mathcal{H}_p} \mu_{pf} c_f \right| \right) \Delta x \le 2.$$
 (34)

This inequality becomes:

$$\frac{-2}{d\Delta t \Delta x} + \sum_{q \in \mathcal{H}_p} \mu_{pq} + \sum_{r \in \mathcal{H}_p} \mu_{pr} - \mu_{pb}
\leq \mu_{pb} - \sum_{f \in \mathcal{H}_p} \mu_{pf} c_f \leq \frac{2}{d\Delta t \Delta x} - \sum_{q \in \mathcal{H}_p} \mu_{pq} - \sum_{r \in \mathcal{H}_p} \mu_{pr} + \mu_{pb}.$$
(35)

The right inequality yields:

$$d\Delta t \left(2 \sum_{q \in \mathcal{H}_p} \mu_{pq} - \sum_{f \in \mathcal{H}_p} \mu_{pr} \left(c_f + 1 \right) \right) \Delta x \le 2, \tag{36}$$

or, more simply:

$$\Delta t \le \frac{1}{d\left(\sum_{q \in \mathcal{H}_p} \mu_{pq} - \frac{1}{2} \sum_{f \in \mathcal{H}_p} \mu_{pr} \left(c_f + 1\right)\right) \Delta x}$$
 (37)

This restriction on the time-step size is always verified if equation (23) holds. On the other hand, the left inequality yields:

$$d\Delta t \left(2 \sum_{q \in \mathcal{H}_p} \mu_{pq} + \sum_{f \in \mathcal{H}_p} \mu_{pf} \left(c_f - 1 \right) - 2 \mu_{pb} \right) \Delta x \le 2, \tag{38}$$

which leads to:

$$\Delta t \le \frac{1}{d \left(\sum_{q \in \mathcal{H}_p} \mu_{pq} + \frac{1}{2} \sum_{f \in \mathcal{H}_p} \mu_{pf} \left(c_f - 1 \right) - \mu_{pb} \right) \Delta x}$$
 (39)

If the inequality in equation (32) holds, then the restriction on the timestep size given in equation (23) is tighter than the one in equation (39).

The last case to analyze is the row of matrix A corresponding to the interior node closest to the boundary (p = b in equation (25)):

$$C_b^{n+1} = \left[1 - d\Delta t \left(\sum_{q \in \mathcal{H}_b} \mu_{bq} \Delta x + \sum_{f \in \mathcal{H}_b} \mu_{bf} c_f \Delta x\right)\right] C_b^n + d\Delta t \sum_{r \in \mathcal{H}_b} \mu_{br} C_r^n \Delta x.$$
(40)

In this case the Gershgorin Theorem yields:

$$\left| \lambda - 1 + d\Delta t \left(\sum_{q \in \mathcal{H}_b} \mu_{bq} + \sum_{f \in \mathcal{H}_b} \mu_{bf} c_f \right) \Delta x \right| \le d\Delta t \sum_{r \in \mathcal{H}_b} \mu_{br} \Delta x, \tag{41}$$

which leads to:

$$-d\Delta t \sum_{r \in \mathcal{H}_b} \mu_{br} \Delta x \le \lambda - 1 + d\Delta t \left(\sum_{q \in \mathcal{H}_b} \mu_{bq} + \sum_{f \in \mathcal{H}_b} \mu_{bf} c_f \right) \Delta x$$

$$\le d\Delta t \sum_{r \in \mathcal{H}_b} \mu_{br} \Delta x. \tag{42}$$

On the one hand, to ensure that $\lambda \le 1$, the right inequality becomes:

$$-\sum_{f \in \mathcal{H}_t} \mu_{bf} \left(c_f + 1 \right) \le 0, \tag{43}$$

which is always true. On the other hand, to have $\lambda \ge -1$, we obtain from the left inequality:

$$d\Delta t \left(2 \sum_{q \in \mathcal{H}_b} \mu_{bq} + \sum_{f \in \mathcal{H}_b} \mu_{bf} \left(c_f - 1 \right) \right) \Delta x \le 2, \tag{44}$$

Note that this inequality is more restrictive than the one in equation (23). From here, equation (17) is straightforwardly derived. \square

It is worth noting that the stability condition in equation (17) is more restrictive than the one in equation (16). Hence, neglecting the boundary conditions (as in the Von Neumann analysis) may lead to a poor guess of the time-step size to obtain the stability of the method. Furthermore, when the self-transfer term is considered, the upper bound for time-step size is even tighter than the one provided in equation (17).

To simplify the formula of the stability criterion for quicker implementation, the symmetry of the neighborhood is employed. We denote the bond length by $m\Delta x$ with $m=1,2,...,\overline{m}$, where $\overline{m}=\delta/\Delta x$ is assumed to be a positive integer for simplicity. If this is not the case, \overline{m} can be replaced with the integer number M such as $M\Delta x$ is the maximum distance from node p of a node with a portion of its cell within the neighborhood of node p itself. In peridynamic models, the value of \overline{m} is often referred to as \overline{m} -ratio. Hence, the stability criterion when the influence of the boundary conditions and the self-transfer term are not considered is given as:

$$\Delta t \le \frac{1}{\frac{m}{m}} \mu(m\Delta x) \Delta x \tag{45}$$

A tighter upper bound for the time-step size is found by considering the influence of the boundary conditions (see equation (17)):

$$\Delta t \le \frac{1}{d\left(2\sum_{m=1}^{\overline{m}}\mu(m\Delta x) + \frac{1}{2}\sum_{m=1}^{\overline{m}}\mu(m\Delta x)(2m-2)\right)\Delta x},$$
(46)

where, given the symmetry of the neighborhood, here we considered only one half of it and multiply the summations by 2. This stability criterion can be further simplified as:

$$\Delta t \le \frac{1}{d \sum_{m=1}^{\overline{m}} \mu(m\Delta x) (m+1) \Delta x}$$
 (47)

The time-step size is bounded even more tightly when the self-transfer term is considered:

$$\Delta t \le \frac{1}{d \left(\sum_{m=1}^{\overline{m}} \mu(m\Delta x) (m+1) + \frac{1}{2} \mu(\Delta x) \right) \Delta x}$$
 (48)

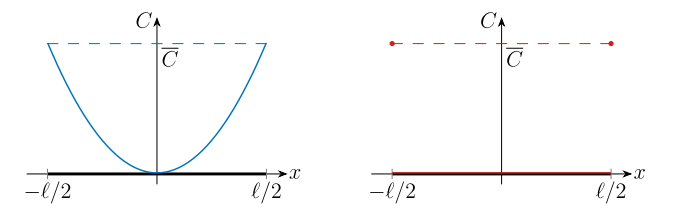
The derived stability condition is analogous to the Courant-Friedrichs-Lewy (CFL) condition in classical convection equations, but it is intrinsically different: a stable Δt is not limited by $\mathcal{O}(\Delta x^2)$ (as in models based on classical diffusion equations) but depends only weakly on Δx for a fixed value of δ . By analyzing the right-hand side of equation (47), one can see that the upper bound for a stable time-step is given by $\mathcal{O}(\delta^2)$ instead. For instance, choosing the kernel $\mu(|\xi|) = |\xi|^{-2}$ (for which $d = D/\delta$) yields:

$$\Delta t \le \frac{\delta}{D \sum_{m=1}^{\overline{m}} \frac{(m+1)}{m^2 \Delta x} + \frac{1}{2\Delta x}} = \frac{\delta}{\mathcal{O}(1/\delta)} = \mathcal{O}(\delta^2). \tag{49}$$

Remark 1. For the case of bi-material diffusion (as used in, for example, PD modeling of corrosion damage [3,53,5,54–58], and ZrC oxidation [59]), the stability criterion derived above can still be used to determine the time-step size by employing the highest diffusivity/dissolvability between the two phases.

4. Convergence studies for diffusion problems with continuous and discontinuous initial conditions

To begin with, we consider the diffusion problem in a homogeneous bar without any phase change. In this section, we will focus on the role of discontinuities in initial conditions in peridynamic problems. Some phenomena require to be modeled with discontinuous initial conditions, such as the oxidation of a zirconium carbide sample which is suddenly exposed to an oxidizing environment [6,7]. To simulate these experimental conditions, we assume that the two ends of the bar are maintained at the maximum concentration of oxygen \overline{C} and that the



- (a) Continuous initial conditions.
- (b) Discontinuous initial conditions.

Fig. 9. Different initial conditions for the 1D diffusion problem without phase change.

initial oxygen concentration is equal to 0 in the whole bar (except the two ends), as depicted in Fig. 9b. However, the surface node method has never been used in a problem evolving in time, let alone with discontinuous initial conditions at the boundary. Therefore, we also analyze the same problem with continuous (quadratic) initial conditions, as shown in Fig. 9a. The analytical solutions to the problem with the initial conditions with and without discontinuities are determined via the method of separation of variables [71]. Thus, we analyze the convergence behaviors in space (with δ fixed) and time to the exact nonlocal solution of the problem with continuous and discontinuous initial conditions.

In what follows, we will use specific units because of the direct applicability of these derivations and results to oxidation-induced damage in the ZrC problem [6,7,72]. The results, however, are independent of these units and the conclusions remain valid for non-dimensionalized form of the problem.

4.1. Analytical solutions

The 1D problem with continuous initial conditions, i.e., a quadratic function (Fig. 9a), is given as:

$$\begin{cases} \frac{\partial C(x,t)}{\partial t} = \int_{\mathcal{H}_x} \mathbf{j}(x,x',t) \, \mathrm{d}x' & \text{for } -\ell/2 < x < \ell/2, \ 0 < t < \infty, \\ C(-\ell/2,t) = C(\ell/2,t) = \overline{C} & \text{for } 0 < t < \infty, \end{cases}$$

$$C(x,0) = \frac{4\overline{C}}{\ell^2} x^2 \qquad \text{for } -\ell/2 < x < \ell/2,$$

$$(50)$$

where ℓ is the length of the rod. The peridynamic solution of this problem is obtained via the method of separation of variables [71]:

$$\frac{\widehat{C}(x,t)}{\overline{C}} = 1 - \sum_{m=1}^{\infty} \frac{32\sin(k_m\ell/2)}{k_m^2\ell^3} \cos(k_m x) \exp(-D\psi t), \tag{51}$$

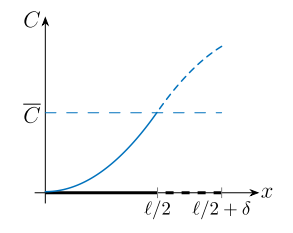
where $k_m = (2m-1)\pi/\ell$ and $\psi = \psi(\delta)$ is the nonlocal factor computed as:

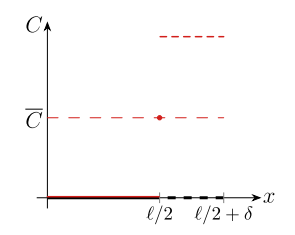
$$\psi(\delta) = \int_{-\delta}^{\delta} \frac{\cos(k_m \xi) - 1}{\delta \xi^2} d\xi$$

$$= \frac{2}{\delta} \left[k_m \text{Si}(k_m \delta) + \frac{\cos(k_m \delta) - 1}{\delta} \right],$$
(52)

where $\xi = x' - x$ and $\operatorname{Si}(y) = \int_0^y \frac{\sin z}{z} \, \mathrm{d}z$ is the sine integral function. Note that in the computation of the nonlocal factor the assumption of an infinite body is made, i.e., the integral is computed assuming a complete horizon region. Therefore, the analytical solution in equation (51) is valid outside of the body as well. This is equivalent to choosing an extrapolation of the unknowns over the fictitious layer that is antisymmetric with respect to the boundary, as shown in Fig. 10a.

Similarly, the 1D problem with discontinuous initial conditions, i.e., the constant zero-valued function (Fig. 9b), is given as:





- (a) Continuous initial conditions.
- (b) Discontinuous initial conditions.

Fig. 10. Antisymmetric extrapolation over the fictitious layer assumed to derive the nonlocal analytical solution for different initial conditions.

Table 1Properties of the rod.

Property	Value
Length of the rod	ℓ = 1 cm
Horizon size	$\delta = 0.05 \text{ cm}$
Classical diffusivity	$D = 1 \text{ cm}^2/\text{s}$
Maximum concentration	$\overline{C} = 1 \text{ mol/cm}^3$

$$\begin{cases} \frac{\partial C(x,t)}{\partial t} = \int\limits_{\mathcal{H}_x} \mathbf{j}(x,x',t) \, \mathrm{d}x' & \text{for } -\ell/2 < x < \ell/2, \ 0 < t < \infty, \\ C(-\ell/2,t) = C(\ell/2,t) = \overline{C} & \text{for } 0 < t < \infty, \\ C(x,0) = 0 & \text{for } -\ell/2 < x < \ell/2. \end{cases}$$
(53)

The peridynamic solution of this problem can be computed as [71]:

$$\frac{\widehat{C}(x,t)}{\overline{C}} = 1 - \sum_{m=1}^{\infty} \frac{4\sin(k_m \ell/2)}{k_m \ell} \cos(k_m x) \exp(-D\psi t), \tag{54}$$

where $k_m = (2m-1)\pi/\ell$ and $\psi = \psi(\delta)$ is the same nonlocal factor of equation (52). As shown in Fig. 10b, the antisymmetric extrapolation over the fictitious layer is assumed to compute the nonlocal factor $\psi(\delta)$.

4.2. Numerical results

The values for the model parameters are shown in Table 1. The same parameters are used for both the continuous and discontinuous initial conditions. These parameters are not realistic, but are used to verify the numerical model. Since the problem is symmetric, we consider only half of the domain and enforce a zero-flux at x = 0 by imposing symmetric boundary conditions as described in [73].

The numerical results, compared to the analytical solution, for the continuous and discontinuous initial conditions are shown in Figs. 11 and 12, respectively. These plots are obtained for a value of the \overline{m} -ratio equal to 4 ($\Delta x = 125~\mu m$) and the time-step size equal to 0.1 ms. This value of the time-step meets the requirement of equation (48) for numerical stability. Moreover, no qualitative differences are visible in the plots if smaller time-steps are chosen. The numerical results are in excellent agreement with their corresponding analytical solutions. This is also observed in the case of discontinuous initial conditions.

Nonetheless, analyzing in more detail the early times of the simulation, we observed that the errors for the discontinuous initial conditions are localized near the boundary and are non-negligible only at the early times of the simulation, as shown for instance in Fig. 13. Furthermore, since the analytical solution is given in the form of an infinite summation of Fourier terms, some inaccuracies arise due to the truncation of higher-order terms, especially when there is a discontinuity in the solution. Therefore, in the following convergence analysis, we study the influence of ignoring the initial time interval of the simulation in the computation of the error for the case with discontinuous initial conditions.

The errors can be computed by averaging the concentration errors in space and taking the maximum error in time:

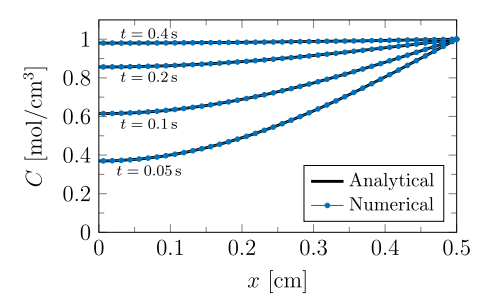


Fig. 11. Numerical results (for $\Delta x = 125~\mu m$ and $\Delta t = 0.1~ms$) and corresponding analytical solution at different times t for the problem with continuous initial conditions.

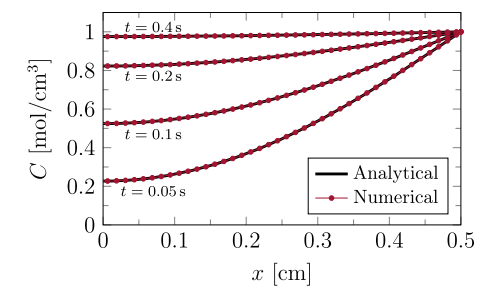


Fig. 12. Numerical results (for a grid spacing $\Delta x = 125 \, \mu \text{m}$ and a time-step size $\Delta t = 0.1 \, \text{ms}$) and corresponding analytical solution at different times t for the problem with discontinuous initial conditions.

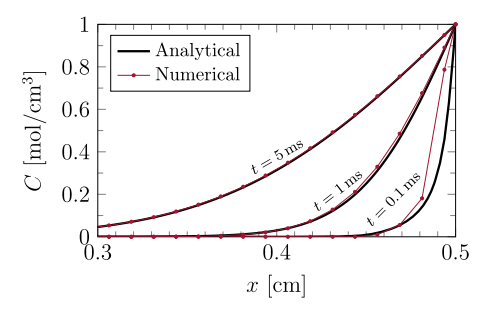


Fig. 13. Example of the behavior of the analytical and numerical solutions near the boundary of the body in the initial time-steps of a simulation with $\Delta x = 125$ μ m and $\Delta t = 0.1$ ms.

$$e = \max_{t_0 \le t \le t_f} \left(\sqrt{\frac{\sum_{p=1}^{N} \left[C(x_p, t) - \hat{C}(x_p, t) \right]^2}{N \, \overline{C}^2}} \right), \tag{55}$$

where t_0 and t_f are respectively the initial and final considered instants of time, C is the numerical result for the degree of freedom of node p, \widehat{C} is the analytical solution evaluated at x_p , and N is the number of degrees of freedom of the model. The error is computed in this way to obtain a single value for each simulation and compare them when the grid spacing or the time-step size are changed. The analytical solution (equation (51) for the continuous initial conditions or equation (54) for the discontinuous ones) is truncated after 200 terms. For what was discussed before, we choose $t_0=0$ s for the problem with continuous initial condition and $t_0=1$ ms for the one with discontinuous initial condition. On the other hand, $t_f=0.5$ s for both cases.

The first convergence analysis was performed with the peridynamic model with the linear extrapolation over the fictitious layer, but the results were not good. For instance, the \overline{m} -convergence behavior of the model with continuous initial conditions shows a low convergence rate, whereas the numerical solution of the problem with discontinuous initial conditions slightly diverges from the nonlocal analytical

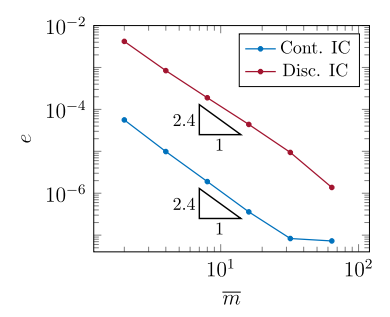


Fig. 14. \overline{m} -convergence (for $\Delta t = 5 \times 10^{-8}$ s) for continuous and discontinuous initial conditions (discontinuous case skips over the first 1 ms).

solution. These poor results are due to the different assumptions that the analytical solution and the numerical model use to extrapolate the concentrations over the fictitious layer: the former one employs an antisymmetric extrapolation, while the latter one a linear extrapolation. Therefore, to obtain reasonable convergence behaviors for the peridynamic diffusion models, we need to use the same type of extrapolation in both analytical and numerical solutions.

Thus, only in the following convergence analyses are the concentrations of the fictitious nodes in the discretized model imposed to be antisymmetric with respect to the concentration of the surface node:

$$C(x_f, t) = 2C(x_s, t) + C(x_m, t),$$
 (56)

where x_f , x_s , and x_m are the coordinates of the fictitious node, the surface node, and the node symmetric to node f with respect to the boundary, respectively. Note that the stability criterion derived in Section 3 is not valid in this case due to the different extrapolations that are assumed. However, following the same steps as shown for the linear extrapolation, one could easily derive the stability criterion also in the case of antisymmetric extrapolation.

We perform a \overline{m} -convergence analysis (grid refinement keeping the value of the horizon δ fixed) for a time-step size $\Delta t = 5 \times 10^{-8}$ s. We chose a very small time-step size to reduce the errors related to the time-integration compared to those related to the space discretization. The values of the \overline{m} -ratio are varied as $\overline{m} = 2^k$, with $k = 1, 2, \ldots, 6$. Fig. 14 shows the results of the \overline{m} -convergence studies, which highlight larger errors in the case discontinuous initial conditions compared to the case with continuous initial conditions. Nevertheless, the errors are considerably small also when a discontinuity is present in the initial conditions. Furthermore, the rate of convergence is not affected by the presence of a discontinuity (when the early times of the simulation are ignored).

Fig. 15 shows the convergence behaviors for different time intervals skipped at the beginning of the simulation. When early times are considered, the maximum errors in time are found in the first time-steps. This is due to the fact that the representation of the discontinuity in the initial conditions is only approximated in the numerical model. On the other hand, when a sufficiently long time interval is ignored, the convergence rate is approximately the same as for the numerical model with continuous initial conditions.

Similarly, we analyze the convergence behavior due to the refinement of the time-step size Δt for a fixed value of grid spacing $\Delta x = 50$ μm , shown in Fig. 16. As in the case of \overline{m} -convergence, the numerical results for the problem with discontinuous initial conditions exhibit the same rate of convergence as those for the problem with continuous initial conditions. However, the numerical errors are higher when a discontinuity is present in the initial conditions. As shown in Fig. 17, the discontinuity in the initial conditions influences only the early times of the simulation.

Several parameters may affect the size of the initial time interval that has to be skipped in the computation of the error to obtain the same convergence rate as the model with continuous initial conditions. Among those parameters, the value of the diffusivity is arguably the

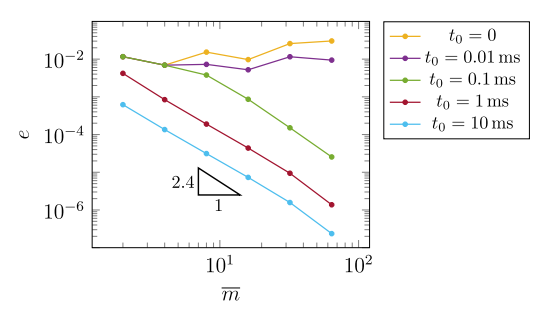


Fig. 15. Influence of initial skipped time interval on the \overline{m} -convergence properties to the analytical solution to the nonlocal problem (all results are for $\Delta t = 5 \times 10^{-8}$ s).

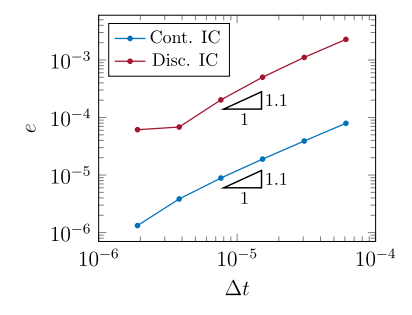


Fig. 16. Time-convergence (for $\Delta x = 50~\mu m$) for continuous and discontinuous initial conditions (discontinuous case skips over the first 1 ms).

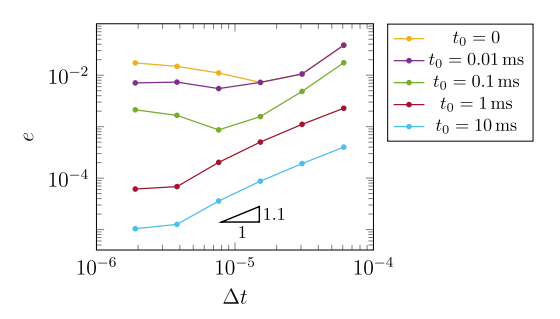


Fig. 17. Influence of initial skipped time interval on the time-convergence properties to the analytical solution to the nonlocal problem (all results are for $\Delta x = 50$ µm).

most influential. Increasing the diffusivity leads to a reduction of the time interval mentioned above. More precisely, the size of the initial time interval ignored to obtain the "expected" convergence behavior is inversely proportional to the diffusivity value.

5. Diffusion problem with moving interface

In this section, the peridynamic model for a bi-material body with a moving interface is analyzed. As pointed out before, the motion of the interface is not related to a condition imposed at the interface itself, but it is part of the peridynamic solution of the problem. Therefore, we are interested in monitoring the accuracy of the numerical results for the position of the interface at each instant of time. Since the analytical solution to this type of nonlocal problem is difficult (if not impossible) to obtain, we use the solution of a manufactured problem instead.

5.1. Manufactured solution

We assume that the manufactured solution is given as:

$$\frac{\widehat{C}(x,t)}{\overline{C}} = 1 + \left(\frac{4}{\ell^2}x^2 - 1\right)\left(1 - \frac{t}{t_f}\right),\tag{57}$$

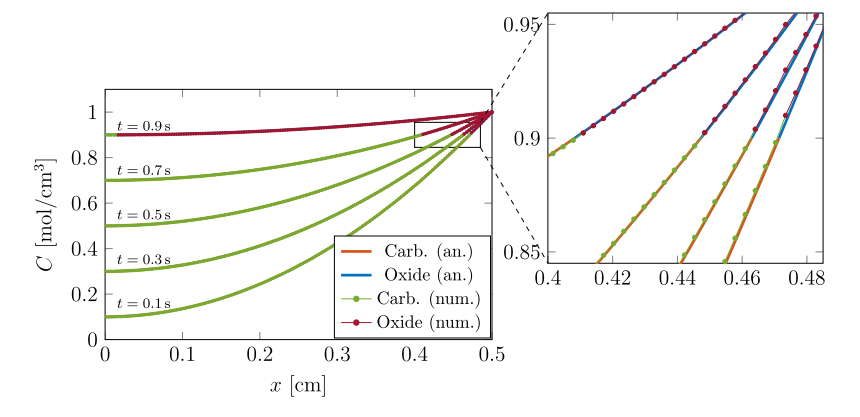


Fig. 18. Numerical results (for a grid spacing $\Delta x = 0.003125$ cm and a time-step size $\Delta t = 1 \times 10^{-5}$ s) and corresponding analytical solution at different times t for the manufactured problem with phase change.

where t_f is the final instant of time in which the solution is equal to $C(x,t) = \overline{C}$. The manufactured solution is plotted in Fig. 18 at different instants of time. Note that equation (57) does not describe the "natural" evolution of the concentration, but the verification of a manufactured problem does not require physically realistic solutions [74]. The manufactured solution is chosen to be symmetric with respect to the origin of the axis, thus we consider only the positive part of the coordinate axis.

The motion of the interface can be described by equalizing equation (57) with the concentration of phase change C_i :

$$\frac{C_i}{\overline{C}} = 1 + \left(\frac{4}{\ell^2} x_i^2 - 1\right) \left(1 - \frac{t}{t_f}\right),\tag{58}$$

where x_i is the interface position. By solving the previous equation for x_i , the position of the interface in time is given as:

$$x_i = \pm \frac{\ell}{2} \sqrt{1 + \left(\frac{C_i}{\overline{C}} - 1\right) \left(\frac{t_f}{t_f - t}\right)},\tag{59}$$

in which we consider only the positive solution for symmetry reasons.

Since the manufactured solution is not the "natural" evolution of the concentration, an external flux has to be "pushed into" the body. This flux can be computed as the remainder of equation (1) as:

$$\overline{J}(x,t) = \frac{\partial C(x,t)}{\partial t} - \int_{\mathcal{H}_x} \mathbf{j}(x,x',t) \, \mathrm{d}x'$$

$$= -\frac{\overline{C}}{t_f} \left(\frac{4}{\ell^2} x^2 - 1 \right) - \int_{\mathcal{H}} d(x,x',t) \, \frac{\widehat{C}(x',t) - \widehat{C}(x,t)}{(x'-x)^2} \, \mathrm{d}x'.$$
(60)

The integral on the right-hand side of the equation depends on the value of the micro-diffusivities obtained with equation (6). Note that the concentration distribution (and, therefore, the phase of each point) is known in each instant of time from the manufactured solution. Hence, the integral can accordingly be split into a sum of integrals with a constant micro-diffusivity $d(x, x', t) = d_k$, where k = 1, 2, 3 (see equation (6)). Here we solve the indefinite integral that can be used to compute the external flux in equation (60):

$$\int d_k \frac{\widehat{C}(x',t) - \widehat{C}(x,t)}{(x'-x)^2} dx'$$

$$= d_k \int \frac{\overline{C}\left[\left(\frac{4}{\ell^2}x'^2 - 1\right) - \left(\frac{4}{\ell^2}x^2 - 1\right)\right]\left(1 - \frac{t}{t_f}\right)}{(x'-x)^2} dx'$$

$$= \frac{4d_k \overline{C}}{\ell^2} \left(1 - \frac{t}{t_f}\right) \int \frac{x'^2 - x^2}{(x'-x)^2} dx'$$

$$= \frac{4d_k \overline{C}}{\ell^2} \left(1 - \frac{t}{t_f}\right) \int \frac{\xi(\xi + 2x)}{\xi^2} d\xi$$
(61)

$$= \frac{4 d_k \overline{C}}{\ell^2} \left(1 - \frac{t}{t_f} \right) \left[\xi + 2x \frac{\xi}{|\xi|} \log(|\xi|) + \text{const.} \right],$$

where $\xi = x' - x$.

5.2. Numerical results

The data used is the same as in Table 1, except for the diffusivity that is chosen to be different in each phase. The following data is thought to be applied in the case of the zirconium carbide oxidation, but the model of the diffusion-reaction phenomenon in a bi-material enhanced with a phase-change mechanism is also applicable to other phenomena with similar characteristics. Since no diffusion occurs in the carbide region (in fact, no concentration of oxygen is present in the carbide), the diffusivity of the carbide phase is $D_c = 0$ cm²/s. On the other hand, the diffusivities of the oxide phase and at the interface are arbitrarily chosen to be $D_o = 1$ cm²/s and $D_i = 0.8$ cm²/s, respectively. Therefore, the three micro-diffusivities of equation (6) are respectively $d_1 = 0$, $d_2 =$ D_i/δ , and $d_3 = D_o/\delta$. The concentration of phase change is arbitrarily chosen to be $C_i = 0.9\overline{C}$. The grid spacing and the time-step size are respectively $\Delta x = 0.003125$ cm ($\overline{m} = 16$) and $\Delta t = 1 \times 10^{-5}$ s. The value for the time-step size is chosen on the basis of the stability criterion in equation (48) by using the diffusivity of the oxide phase in the formula (see Remark 1).

The analytical solution of the manufactured problem is computed by using the interface position determined in equation (59) to change the diffusivity of the points. In the discretized model, however, there is no clear way to know precisely the position of the interface when it lies between two adjacent nodes. Therefore, the position of the interface is chosen to be in the middle point between the two adjacent carbide and oxide nodes. The obtained interface position is used to compute the external flux at each node with equations (60) and (61). The fluxes at the nodes can be gathered in the flux vector $\overline{\bf J}$ and the system of equations to solve becomes:

$$\mathbf{C}^{n+1} = \mathbf{A} \, \mathbf{C}^n + \overline{\mathbf{J}} \,. \tag{62}$$

The numerical results are shown at different instants of time in Fig. 18, and they are compared with the analytical (manufactured) solution. The numerical and analytical solutions are in good agreement throughout the whole timespan. It is also interesting to analyze the motion of the interface in the numerical model with respect to the analytical solution in equation (59). Fig. 19 shows that the position of the interface in the numerical model and the manufactured solution are very close to one another at any instant of time. Therefore, the peridynamic model has been shown to be effective in capturing the motion of the interface as a result of the diffusivities of the different phases.

An interesting extension of the work shown here is to consider the moving interface problem with discontinuities. Such an example is considered in [59], in which a peridynamic model of zirconium carbide

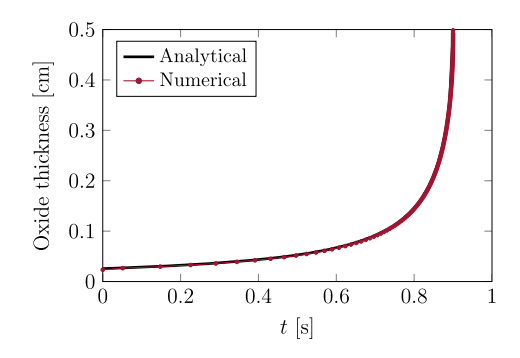


Fig. 19. Numerical results and corresponding analytical solution of the position of the interface for the manufactured problem with phase change.

oxidation is used to simulate the effect of cracks induced by the expansion of the oxide in the outer layer. Comparison of PD results with experimental observations shows an excellent agreement between the two.

6. Discussion on the extension to 2D and 3D problems

In this work, we considered only 1D transient diffusion problems for simplicity's sake. However, we believe that all the obtained results are also valid for 2D and 3D peridynamic diffusion problems. The equations for a 2D or 3D peridynamic transient diffusion problem are presented in Section 3 of [59], and are very similar to the equation governing diffusion in a 1D peridynamic body. In fact, the only difference is that the position of the points/nodes is determined by a vector instead of a scalar value.

It is common practice to derive the stability criterion for numerical methods in 1D problems and then extend it to higher-dimension problems (see, for instance, [75,60]). We therefore use equation (17) in Section 3 for the generalization. The linear Taylor-based extrapolation method for the 3D case used to determine the concentration at a fictitious node \mathbf{x}_t at time t yields [14,15,47]:

$$C(\mathbf{x}_{f},t) \approx C(\mathbf{x}_{s},t) + \left(x_{f} - x_{s}\right) \frac{\partial C(\mathbf{x}_{s},t)}{\partial x} + \left(y_{f} - y_{s}\right) \frac{\partial C(\mathbf{x}_{s},t)}{\partial y}$$

$$+ \left(z_{f} - z_{s}\right) \frac{\partial C(\mathbf{x}_{s},t)}{\partial z}$$

$$\approx \left(1 + \frac{x_{f} - x_{b}}{x_{s} - x_{b}} + \frac{y_{f} - y_{b}}{y_{s} - y_{b}} + \frac{z_{f} - z_{b}}{z_{s} - z_{b}}\right) C(\mathbf{x}_{s},t)$$

$$- \left(\frac{x_{f} - x_{s}}{x_{s} - x_{b}} + \frac{y_{f} - y_{s}}{y_{s} - y_{b}} + \frac{z_{f} - z_{s}}{z_{s} - z_{b}}\right) C(\mathbf{x}_{b},t)$$

$$\approx \left(1 + c_{f}\right) C(\mathbf{x}_{s},t) - c_{f} C(\mathbf{x}_{b},t),$$
(63)

where node \mathbf{x}_s is the surface node closest to node \mathbf{x}_f , node \mathbf{x}_b is the real node closest to node \mathbf{x}_s , and the derivatives are approximated by the finite difference method as shown in equation (10). Note that equation (63) is also valid in 1D with $c_f = \frac{x_f - x_s}{x_s - x_b}$ and in 2D with $c_f = \frac{x_f - x_s}{y_s - y_b} + \frac{y_f - y_s}{y_s - y_b}$. Therefore, since the governing equations in 2D or 3D diffusion problems have the same "structure" as those in 1D problems, we deduce that the stability criterion generalized for a higher-dimension transient diffusion problem is as follows:

$$\Delta t \le \frac{1}{d\left(\sum_{a \in \mathcal{H}_b} \mu_{bq} + \frac{1}{2} \sum_{f \in \mathcal{H}_b} \mu_{bf} \left(c_f - 1\right)\right) \Delta x},\tag{64}$$

where $c_f = \frac{x_f - x_s}{x_s - x_b}$ in 1D, $c_f = \frac{x_f - x_s}{x_s - x_b} + \frac{y_f - y_s}{y_s - y_b}$ in 2D, and $c_f = \frac{x_f - x_s}{x_s - x_b} + \frac{y_f - y_s}{y_s - y_b} + \frac{z_f - z_b}{z_s - z_b}$ in 3D. The nodes near the corners of the body, i.e., the nodes with the highest number of fictitious nodes inside their neighborhood, are likely to provide the smallest upper bound for the time-step size.

As shown in Section 4 for a 1D peridynamic transient diffusion problem, a discontinuity at the boundary in the initial conditions affects the numerical convergence rate only at the very early stages of the simulation. This is due to the fact that the discontinuity is quickly "smoothed out" by the diffusion phenomenon that tends to reduce the high gradients of concentration, as shown for example in the analytical solution depicted in Fig. 13. This effect of diffusion is obviously independent of the considered number of dimensions of the model. Therefore, it is expected that the same conclusions that were obtained in the 1D case are also valid in the 2D and 3D cases.

In this work, we quantitatively evaluated the accuracy of the position of the autonomously moving interface in a 1D peridynamic diffusion problem when compared to a manufactured solution. Except for the (possibly) slightly higher errors due to the numerical integration of the peridynamic operator in 2D and 3D problems, we expect that the accuracy of the position of the moving interface should be similar to that obtained in the proposed 1D numerical example. Furthermore, the 2D and 3D peridynamic diffusion models for a bi-material have already been used to successfully reproduce complex phenomena, such as corrosion [3,53,5,54–58] and zirconium carbide oxidation [59]. These works show that the peridynamic modeling in 1D, 2D, and 3D cases is capable of accurately predicting the motion of interfaces in excellent agreement with experimental observations.

7. Conclusions

In this work, we analyzed several numerical aspects in the peridynamic model for a diffusion problem with and without moving interface. To this end, we considered the example of the zirconium carbide oxidation for the choice of initial/boundary conditions and material properties, but the results may be easily generalized to other physical phenomena with similar characteristics. Moreover, the boundary conditions are imposed, for the first time, by means of the surface node method in a problem evolving over time.

It is well-known that explicit numerical methods for time integration of the diffusion equation incur in instability unless the time-step size is sufficiently small. The Von Neumann method can provide a first guess for the time-step size allowed to obtain the stability of the numerical method, but this method does not consider the influence of the boundary conditions. Thanks to the eigenvalue technique for stability analysis and the Gershgorin Theorem, we have determined a more general stability criterion for peridynamic diffusion models that takes into account the numerical method as a whole, including the effect of the boundary conditions. In fact, considering the boundary conditions provides a tighter upper bound for the time-step size to obtain the stability of the numerical method.

Then, we showed the numerical results and the convergence to the exact peridynamic solution of a diffusion problem with continuous and discontinuous initial conditions in a homogeneous body without phase change. The presence of a discontinuity in the initial conditions affects the numerical approximation only in the early stages of the simulation. When a sufficiently long initial time interval is ignored, the convergence rate of the model with discontinuous initial conditions is the same as that of the model with continuous initial conditions. This fact has been verified for both \overline{m} -convergence (grid refinement while keeping the horizon size δ constant) and time-convergence analysis.

Furthermore, we solved a diffusion problem in a bi-material enhanced with a phase-change model. This model makes use of the diffusion equation to determine both the concentration of the considered species within the body and the position of the interface between different phases. In fact, the phase-change is driven by the concentration of the species itself. The numerical results, in terms of concentration profile and position of the interface, are in good agreement with the analytical (manufactured) solution. These analyses pave the way for the modeling of more complex phenomena, including reaction-induced

damage mechanisms that can be easily introduced within the peridynamic framework.

Data availability

All data is presented in the content of the manuscript.

Acknowledgements

U. Galvanetto and M. Zaccariotto would like to acknowledge the support they received from University of Padova under the PRIN 2017 research project "DEVISU" (2017ZX9X4K) and from University of Padova under the research project BIRD2020 NR. 202824/20. The research of A. Larios was supported in part by NSF grants DMS-2206762 and CMMI-1953346, and USGS grant G23AC00156-00. The research of F. Bobaru was supported in part by the NSF grant CMMI-1953346.

References

- A. Visintin, Introduction to Stefan-type problems, in: Handbook of Differential Equations: Evolutionary Equations, vol. 4, 2008, pp. 377–484.
- [2] S. Mitchell, M. Vynnycky, On the numerical solution of two-phase Stefan problems with heat-flux boundary conditions, J. Comput. Appl. Math. 264 (2014) 49–64, https://doi.org/10.1016/j.cam.2014.01.003.
- [3] Z. Chen, F. Bobaru, Peridynamic modeling of pitting corrosion damage, J. Mech. Phys. Solids 78 (2015) 352–381, https://doi.org/10.1016/j.jmps.2015.02.015.
- [4] M. Khalid, M. Zubair, M. Ali, An analytical method for the solution of two phase Stefan problem in cylindrical geometry, Appl. Math. Comput. 342 (2019) 295–308, https://doi.org/10.1016/j.amc.2017.09.013.
- [5] S. Jafarzadeh, Z. Chen, F. Bobaru, Peridynamic modeling of repassivation in pitting corrosion of stainless steel, Corrosion 74 (4) (2018) 393–414, https://doi.org/10. 5006/2615.
- [6] C. Gasparrini, R. Podor, D. Horlait, R. Chater, W. Lee, Zirconium carbide oxidation: Maltese cross formation and interface characterization, Oxid. Met. 88 (2017) 509–519, https://doi.org/10.1007/s11085-016-9672-6.
- [7] C. Gasparrini, R. Chater, D. Horlait, L. Vandeperre, W. Lee, Zirconium carbide oxidation: kinetics and oxygen diffusion through the intermediate layer, J. Am. Ceram. Soc. 101 (6) (2018) 2638–2652, https://doi.org/10.1111/jace.15479.
- [8] S. Silling, Reformulation of elasticity theory for discontinuities and long-range forces, J. Mech. Phys. Solids 48 (1) (2000) 175–209, https://doi.org/10.1016/ S0022-5096(99)00029-0.
- [9] S. Silling, M. Epton, O. Weckner, J. Xu, E. Askari, Peridynamic states and constitutive modeling, J. Elast. 88 (2) (2007) 151–184, https://doi.org/10.1007/s10659-007-9125-1.
- [10] R. Macek, S. Silling, Peridynamics via finite element analysis, Finite Elem. Anal. Des. 43 (15) (2007) 1169–1178, https://doi.org/10.1016/j.finel.2007.08.012.
- [11] F. Bobaru, Y. Ha, Adaptive refinement and multiscale modeling in 2D peridynamics, J. Multiscale Comput. Eng. 9 (6) (2011) 635–659, https://doi.org/10.1615/IntJMultCompEng.2011002793.
- [12] W. Liu, J. Hong, Discretized peridynamics for linear elastic solids, Comput. Mech. 50 (5) (2012) 579–590, https://doi.org/10.1007/s00466-012-0690-1.
- [13] Q. Le, F. Bobaru, Surface corrections for peridynamic models in elasticity and fracture, Comput. Mech. 61 (4) (2018) 499–518, https://doi.org/10.1007/s00466-017-1460.1
- [14] F. Scabbia, M. Zaccariotto, U. Galvanetto, A novel and effective way to impose boundary conditions and to mitigate the surface effect in state-based peridynamics, Int. J. Numer. Methods Eng. 122 (20) (2021) 5773–5811, https://doi.org/10.1002/ nme 6773
- [15] F. Scabbia, M. Zaccariotto, U. Galvanetto, A new method based on Taylor expansion and nearest-node strategy to impose Dirichlet and Neumann boundary conditions in ordinary state-based peridynamics, Comput. Mech. 70 (1) (2022) 1–27, https:// doi.org/10.1007/s00466-022-02153-2.
- [16] B. Kilic, Peridynamic theory for progressive failure prediction in homogeneous and heterogeneous materials, Ph.D. thesis, 2008, repository.arizona.edu/handle/10150/ 193658.
- [17] E. Madenci, E. Oterkus, Peridynamic Theory and Its Applications, vol. 17, Springer, 2014.
- [18] E. Oterkus, Peridynamic theory for modeling three-dimensional damage growth in metallic and composite structures, Ph.D. thesis, 2010, repository.arizona.edu/ handle/10150/145366
- [19] F. Bobaru, J. Foster, P. Geubelle, S. Silling, Handbook of Peridynamic Modeling, CRC Press, 2016, books.google.it/books?id=cBgNDgAAQBAJ.
- [20] J. Mitchell, S. Silling, D. Littlewood, A position-aware linear solid constitutive model for peridynamics, J. Mech. Mater. Struct. 10 (5) (2015) 539–557, https://doi.org/ 10.2140/jomms.2015.10.539.

- [21] L. Lopez, S. Pellegrino, A space-time discretization of a nonlinear peridynamic model on a 2D lamina, Comput. Math. Appl. 116 (2022) 161–175, https://doi.org/10. 1016/j.camwa.2021.07.004.
- [22] U. Galvanetto, T. Mudric, A. Shojaei, M. Zaccariotto, An effective way to couple fem meshes and peridynamics grids for the solution of static equilibrium problems, Mech. Res. Commun. 76 (2016) 41–47, https://doi.org/10.1016/j.mechrescom. 2016.06.006.
- [23] A. Shojaei, T. Mudric, M. Zaccariotto, U. Galvanetto, A coupled meshless finite point/peridynamic method for 2D dynamic fracture analysis, Int. J. Mech. Sci. 119 (2016) 419–431, https://doi.org/10.1016/j.ijmecsci.2016.11.003.
- [24] M. Zaccariotto, D. Tomasi, U. Galvanetto, An enhanced coupling of PD grids to FE meshes, Mech. Res. Commun. 84 (2017) 125–135, https://doi.org/10.1016/j. mechrescom.2017.06.014.
- [25] M. Zaccariotto, T. Mudric, D. Tomasi, A. Shojaei, U. Galvanetto, Coupling of FEM meshes with peridynamic grids, Comput. Methods Appl. Mech. Eng. 330 (2018) 471–497, https://doi.org/10.1016/j.cma.2017.11.011.
- [26] T. Ni, M. Zaccariotto, Q. Zhu, U. Galvanetto, Coupling of FEM and ordinary state-based peridynamics for brittle failure analysis in 3D, Mech. Adv. Mat. Struct. 28 (9) (2021) 875–890, https://doi.org/10.1080/15376494.2019.1602237.
- [27] W. Sun, J. Fish, Superposition-based coupling of peridynamics and finite element method, Comput. Mech. 64 (1) (2019) 231–248, https://doi.org/10.1007/s00466-019-01668-5.
- [28] A. Pagani, E. Carrera, Coupling three-dimensional peridynamics and high-order onedimensional finite elements based on local elasticity for the linear static analysis of solid beams and thin-walled reinforced structures, Int. J. Numer. Methods Eng. 121 (22) (2020) 5066–5081, https://doi.org/10.1002/nme.6510.
- [29] A. Pagani, M. Enea, E. Carrera, Quasi-static fracture analysis by coupled three-dimensional peridynamics and high order one-dimensional finite elements based on local elasticity, Int. J. Numer. Methods Eng. 123 (4) (2022) 1098–1113, https://doi.org/10.1002/nme.6890.
- [30] G. Ongaro, R. Bertani, U. Galvanetto, A. Pontefisso, M. Zaccariotto, A multiscale peridynamic framework for modelling mechanical properties of polymer-based nanocomposites, Eng. Fract. Mech. 274 (2022) 108751, https://doi.org/10.1016/ j.engfracmech.2022.108751.
- [31] G. Ongaro, P. Seleson, U. Galvanetto, T. Ni, M. Zaccariotto, Overall equilibrium in the coupling of peridynamics and classical continuum mechanics, Comput. Methods Appl. Mech. Eng. 381 (2021) 113515, https://doi.org/10.1016/j.cma.2020.113515.
- [32] F. Bobaru, M. Yang, L. Alves, S. Silling, E. Askari, J. Xu, Convergence, adaptive refinement, and scaling in 1d peridynamics, Int. J. Numer. Methods Eng. 77 (6) (2009) 852–877, https://doi.org/10.1002/nme.2439.
- [33] S. Silling, D. Littlewood, P. Seleson, Variable horizon in a peridynamic medium, J. Mech. Mater. Struct. 10 (5) (2015) 591–612, https://doi.org/10.2140/jomms.2015. 10.591.
- [34] H. Ren, X. Zhuang, Y. Cai, T. Rabczuk, Dual-horizon peridynamics, Int. J. Numer. Methods Eng. 108 (12) (2016) 1451–1476, https://doi.org/10.1002/nme.5257.
- [35] H. Ren, X. Zhuang, T. Rabczuk, Dual-horizon peridynamics: a stable solution to varying horizons, Comput. Methods Appl. Mech. Eng. 318 (2017) 762–782, https://doi.org/10.1016/j.cma.2016.12.031.
- [36] S. Prudhomme, P. Diehl, On the treatment of boundary conditions for bond-based peridynamic models, Comput. Methods Appl. Mech. Eng. 372 (2020) 113391, https://doi.org/10.1016/j.cma.2020.113391.
- [37] J. Chen, P. Qingdao, Y. Jiao, W. Jiang, Y. Zhang, Peridynamics boundary condition treatments via the pseudo-layer enrichment method and variable horizon approach, Math. Mech. Solids 26 (5) (2021) 631–666, https://doi.org/10.1177/1081286520961144.
- [38] W. Gerstle, N. Sau, S. Silling, Peridynamic modeling of plain and reinforced concrete structures, in: 18th International Conference on Structural Mechanics in Reactor Technology, 2005, repository.lib.ncsu.edu/handle/1840.20/31420.
- [39] S. Oterkus, E. Madenci, A. Agwai, Peridynamic thermal diffusion, J. Comput. Phys. 265 (2014) 71–96, https://doi.org/10.1016/j.jcp.2014.01.027.
- [40] S. Oterkus, Peridynamics for the solution of multiphysics problems, Ph.D. thesis, 2015, repository.arizona.edu/handle/10150/555945.
- [41] Z. Chen, F. Bobaru, Selecting the kernel in a peridynamic formulation: a study for transient heat diffusion, Comput. Phys. Commun. 197 (2015) 51–60, https://doi. org/10.1016/j.cpc.2015.08.006.
- [42] G. Sarego, Q. Le, F. Bobaru, M. Zaccariotto, U. Galvanetto, Linearized state-based peridynamics for 2-d problems, Int. J. Numer. Methods Eng. 108 (10) (2016) 1174–1197, https://doi.org/10.1002/nme.5250.
- [43] Z. Chen, D. Bakenhus, F. Bobaru, A constructive peridynamic kernel for elasticity, Comput. Methods Appl. Mech. Eng. 311 (2016) 356–373, https://doi.org/10.1016/ j.cma.2016.08.012.
- [44] E. Madenci, S. Oterkus, Ordinary state-based peridynamics for plastic deformation according to von Mises yield criteria with isotropic hardening, J. Mech. Phys. Solids 86 (2016) 192–219, https://doi.org/10.1016/j.jmps.2015.09.016.
- [45] J. Zhao, S. Jafarzadeh, Z. Chen, F. Bobaru, An algorithm for imposing local boundary conditions in peridynamic models on arbitrary domains, https://doi.org/10.31224/ osf.io/7z8qr, 2020.
- [46] W. Dong, H. Liu, J. Du, X. Zhang, M. Huang, Z. Li, Z. Chen, F. Bobaru, A peridynamic approach to solving general discrete dislocation dynamics problems in plasticity and fracture: Part I. Model description and verification, Int. J. Plast. 157 (2022) 103401, https://doi.org/10.1016/j.ijplas.2022.103401.

- [47] F. Scabbia, M. Zaccariotto, U. Galvanetto, A new surface node method to accurately model the mechanical behavior of the boundary in 3D state-based peridynamics, J. Peridyn. Nonlocal Model. (2023) 1–35, https://doi.org/10.1007/s42102-022-00094-1.
- [48] F. Bobaru, M. Duangpanya, The peridynamic formulation for transient heat conduction, Int. J. Heat Mass Transf. 53 (19-20) (2010) 4047–4059, https://doi.org/10.1016/j.ijheatmasstransfer.2010.05.024.
- [49] F. Bobaru, M. Duangpanya, A peridynamic formulation for transient heat conduction in bodies with evolving discontinuities, J. Comput. Phys. 231 (7) (2012) 2764–2785, https://doi.org/10.1016/j.jcp.2011.12.017.
- [50] J. Guermond, P. Minev, J. Shen, An overview of projection methods for incompressible flows, Comput. Methods Appl. Mech. Eng. 195 (44–47) (2006) 6011–6045, https://doi.org/10.1016/j.cma.2005.10.010.
- [51] D. Shirokoff, R. Rosales, An efficient method for the incompressible Navier–Stokes equations on irregular domains with no-slip boundary conditions, high order up to the boundary, J. Comput. Phys. 230 (23) (2011) 8619–8646, https://doi.org/10. 1016/j.jcp.2011.08.011.
- [52] R. Lehoucq, S. Silling, Force flux and the peridynamic stress tensor, J. Mech. Phys. Solids 56 (4) (2008) 1566–1577, https://doi.org/10.1016/j.jmps.2007.08.004.
- [53] Z. Chen, G. Zhang, F. Bobaru, The influence of passive film damage on pitting corrosion, J. Electrochem. Soc. 163 (2) (2015) C19, https://doi.org/10.1149/2. 0521602ies.
- [54] S. Jafarzadeh, Z. Chen, F. Bobaru, Peridynamic modeling of intergranular corrosion damage, J. Electrochem. Soc. 165 (7) (2018) C362, https://doi.org/10.1149/2.0821807jes.
- [55] S. Jafarzadeh, Z. Chen, F. Bobaru, Computational modeling of pitting corrosion, Corros. Rev. 37 (5) (2019) 419–439, https://doi.org/10.1515/corrrev-2019-0049.
- [56] S. Jafarzadeh, Z. Chen, S. Li, F. Bobaru, A peridynamic mechano-chemical damage model for stress-assisted corrosion, Electrochim. Acta 323 (2019) 134795, https://doi.org/10.1016/j.electacta.2019.134795.
- [57] J. Zhao, S. Jafarzadeh, M. Rahmani, Z. Chen, Y. Kim, F. Bobaru, A peridynamic model for galvanic corrosion and fracture, Electrochim. Acta 391 (2021) 138968, https://doi.org/10.1016/j.electacta.2021.138968.
- [58] S. Jafarzadeh, J. Zhao, M. Shakouri, F. Bobaru, A peridynamic model for crevice corrosion damage, Electrochim. Acta 401 (2022) 139512, https://doi.org/10.1016/ j.electacta.2021.139512.
- [59] F. Scabbia, C. Gasparrini, M. Zaccariotto, U. Galvanetto, A. Larios, F. Bobaru, Moving interfaces in peridynamic diffusion models and influence of discontinuous initial conditions: numerical stability and convergence, 2023, Submitted for publication.
- [60] S. Silling, E. Askari, A meshfree method based on the peridynamic model of solid mechanics, Comput. Struct. 83 (17–18) (2005) 1526–1535, https://doi.org/10.1016/j.compstruc.2004.11.026.
- [61] P. Seleson, Improved one-point quadrature algorithms for two-dimensional peridynamic models based on analytical calculations, Comput. Methods Appl. Mech. Eng. 282 (2014) 184–217, https://doi.org/10.1016/j.cma.2014.06.016.

- [62] F. Scabbia, M. Zaccariotto, U. Galvanetto, Accurate computation of partial volumes in 3D peridynamics, Eng. Comput. 39 (1) (2023) 959–991, https://doi.org/10.1007/ s00366-022-01725-3.
- [63] Q. Du, L. Tian, X. Zhao, A convergent adaptive finite element algorithm for nonlocal diffusion and peridynamic models, SIAM J. Numer. Anal. 51 (2) (2013) 1211–1234, https://doi.org/10.1137/120871638.
- [64] Q. Du, L. Ju, L. Tian, K. Zhou, A posteriori error analysis of finite element method for linear nonlocal diffusion and peridynamic models, Math. Comput. 82 (284) (2013) 1889–1922, https://doi.org/10.1090/S0025-5718-2013-02708-1.
- [65] S. Jafarzadeh, A. Larios, F. Bobaru, Efficient solutions for nonlocal diffusion problems via boundary-adapted spectral methods, J. Peridyn. Nonlocal Model. 2 (1) (2020) 85–110, https://doi.org/10.1007/s42102-019-00026-6.
- [66] S. Jafarzadeh, L. Wang, A. Larios, F. Bobaru, A fast convolution-based method for peridynamic transient diffusion in arbitrary domains, Comput. Methods Appl. Mech. Eng. 375 (2021) 113633, https://doi.org/10.1016/j.cma.2020.113633.
- [67] P. Seleson, M. Parks, M. Gunzburger, R. Lehoucq, Peridynamics as an upscaling of molecular dynamics, Multiscale Model. Simul. 8 (1) (2009) 204–227, https:// doi.org/10.1137/09074807X.
- [68] L. Lapidus, G. Pinder, Numerical Solution of Partial Differential Equations in Science and Engineering, John Wiley & Sons, 2011.
- [69] Q. Guan, M. Gunzburger, Stability and convergence of time-stepping methods for a nonlocal model for diffusion, Discrete Contin. Dyn. Syst., Ser. B 20 (5) (2015), https://doi.org/10.3934/dcdsb.2015.20.1315.
- [70] Q. Guan, M. Gunzburger, Stability and accuracy of time-stepping schemes and dispersion relations for a nonlocal wave equation, Numer. Methods Partial Differ. Equ. 31 (2) (2015) 500–516, https://doi.org/10.1002/num.21931.
- [71] Z. Chen, X. Peng, S. Jafarzadeh, F. Bobaru, Analytical solutions of peridynamic equations. Part I: transient heat diffusion, J. Peridyn. Nonlocal Model. 4 (3) (2022) 303–335, https://doi.org/10.1007/s42102-022-00080-7.
- [72] F. Scabbia, M. Zaccariotto, U. Galvanetto, F. Bobaru, Peridynamic simulation of elastic wave propagation by applying the boundary conditions with the surface node method, in: III Aerospace PhD-Days, AIDAA, 2023.
- [73] A. Yaghoobi, M. Chorzepa, Formulation of symmetry boundary modeling in non-ordinary state-based peridynamics and coupling with finite element analysis, Math. Mech. Solids 23 (8) (2018) 1156–1176, https://doi.org/10.1177/ 1081286517711495.
- [74] P. Roache, The method of manufactured solutions for code verification, in: Computer Simulation Validation, Springer, 2019, pp. 295–318.
- [75] S. Larsson, V. Thomée, Partial Differential Equations with Numerical Methods, vol. 45, Springer, 2003.